Nano Energy 78 (2020) 105293

Contents lists available at ScienceDirect

Nano Energy

journal homepage: http://www.elsevier.com/locate/nanoen

"Soft on rigid" nanohybrid as the self-supporting multifunctional cathode electrocatalyst for high-performance lithium-polysulfide batteries

Jiayi Wang [a,b,1], Dan Luo [c,1], Junhua Li [b], Yongguang Zhang [a,b,*], Yan Zhao [b], Guofu Zhou [d], Lingling Shui [a], Zhongwei Chen [c,**], Xin Wang [a,d,***]

[a] School of Information and Optoelectronic Science and Engineering & International Academy of Optoelectronics at Zhaoqing, South China Normal University, Guangzhou, 510006, China
[b] School of Materials Science and Engineering, Hebei University of Technology, Tianjin, 300130, China
[c] Department of Chemical Engineering, University of Waterloo, Waterloo, ON, Canada, N2L 3G1
[d] South China Academy of Advanced Optoelectronics, South China Normal University, Guangdong, 510006, China

ARTICLE INFO

Keywords:
Lithium polysulfide batteries
Electrocatalyst
TiO_2
Oxygen vacancies
Electrochemical performance

ABSTRACT

Lithium-sulfur (Li–S) batteries have been deemed as next-generation large-scale energy storage devices. However, the severe shuttle effect and sluggish conversion kinetics of lithium polysulfides significantly impede the commercialization of Li–S batteries. Herein, a unique "soft on rigid" composite consist of oxygen-deficient and Co cluster-decorated TiO_2 nanofibers with carbon nanofibers (CNF), embedding numerous Co nanoparticles (denoted as "Co–TiO_{2-x}/CNF") is developed as a high-performance self-supporting multifunctional cathode electrocatalyst. The Co–TiO_{2-x}/CNF offers vast surface area and enlarged porosity to homogenize sulfur distribution and enhance sulfur immobilization. The oxygen deficient Co–TiO_{2-x} fiber and CNF establish a three-dimensional conductive framework, which accelerates electron and ion transportation within the electrode. Meanwhile, the introduction of Co clusters significantly regulate the Ti d-band center and thereby improving the Li_2S_6 adsorbability. Benefiting from these synergistic features, the Li_2S_6/Co–TiO_{2-x}/CNF electrode delivers outstanding cycling stability (capacity fading rate of 0.03% per cycle over 500 cycles) and an improved rate capability (743 mAh g^{-1} at 3.0C). This design strategy based on synergy engineering could also open up new possibilities for the practical application of high performance Li–S batteries and promote the material design in related energy storage fields.

1. Introduction

Among many competing battery concepts, lithium-sulfur (Li–S) batteries have great promise for next-generation large-scale electric energy storage. Li–S batteries have a five-fold increase in theoretical energy density (2600 Wh kg^{-1}) than commercial lithium ion batteries, and thus may replace current lithium ion batteries [1–3]. Furthermore, sulfur has many attractive features, including low cost, natural abundance, nontoxicity, and environmental friendliness [4–8]. Nonetheless, the practical application of Li–S batteries is still hampered by some intractable obstructions, such as the insulating property of sulfur and its final discharging products (Li_2S_2/Li_2S), the large volume expansion (80%) during lithiation, and the high dissolution of lithium polysulfide (LiPS) intermediates (Li_2S_n, $2 < n \leq 8$) [9–13]. In addition, the electrochemical conversion kinetics from LiPS to Li_2S_2/Li_2S is limited [14,15]. These issues lead to low sulfur utilization, rapid capacity decay, and inferior rate property [16–20].

To resolve these challenges, extensive research efforts have been aimed at the development of sulfur host materials, the modification of separator, and the exploration of electrolyte [21–23]. Although these

* Corresponding author. School of Information and Optoelectronic Science and Engineering & International Academy of Optoelectronics at Zhaoqing, South China Normal University, Guangzhou, 510006, China.
** Corresponding author.
*** Corresponding author. School of Information and Optoelectronic Science and Engineering & International Academy of Optoelectronics at Zhaoqing, South China Normal University, Guangzhou, 510006, China.
E-mail addresses: yongguangzhang@hebut.edu.cn (Y. Zhang), zhwchen@uwaterloo.ca (Z. Chen), wangxin@scnu.edu.cn (X. Wang).
[1] The authors contributed equally to this work.

https://doi.org/10.1016/j.nanoen.2020.105293
Received 12 July 2020; Received in revised form 3 August 2020; Accepted 11 August 2020
Available online 20 August 2020

approaches have achieved substantial progress, enhancing the performance of Li–S batteries still faces massive challenges. Recently, a concept regarding polysulfides conversion catalysts has been used to accelerate the redox reaction, and this approach can mitigate the dissolution of LiPS in the electrolyte and impede the accumulation of polysulfides on the sulfur electrode [24,25]. Polar metal oxides, sulfides, carbides, hydroxide, and metal-organic frameworks have attracted tremendous attention as conversion catalysts because of their intrinsic catalytic activity. Specifically, they provide abundant adsorption sites for chemically anchoring LiPS [26–32]. Among these polar materials, TiO_2 has been used as a sulfur host cathode with strong LiPS confinement, which is able to significantly inhibit the shuttling effect [33]. A recent study found that manipulating the valence state of titanium, accompanied by the introduction of oxygen vacancies, is a capable approach for achieving improved catalytic effect on polysulfide reaction kinetics to obtain a remarkable electrochemical performance [34]. Although there have been many reports of defective materials in the application of Li–S batteries, there are still many areas for improvement. As far as TiO_2 is concerned, although the adsorption capacity of TiO_2 containing oxygen deficiencies has been improved compared to perfect TiO_2, its LiPS catalytic ability and electron conductivity are still unsatisfied, resulting in poor reaction kinetics. Meanwhile, the unsaturated Ti atoms associated with oxygen defect sites are highly reactive, which may be combined with polysulfides, leading to the fast decay of catalytic activity. For this reason, it is still necessary to synchronously adjust the defect structure and the electronic structure to further improve its adsorption and catalytic capabilities for accelerated reaction kinetics.

In addition to improving the catalytic conversion ability through the design of the sulfur host, studies have shown that it is also effective to use soluble polysulfides as active materials [35]. When soluble polysulfide is used as the active material, the initial reaction changes from the traditional solid-liquid-solid reaction to the liquid-solid reaction, which promotes the uniform deposition of sulfur during the first discharge and accelerate the reaction kinetics for improved active material utilization, thereby enhancing the electrochemical performance. For example, Shang et al. employed Mo_2C-decorated N-doping carbon nanofibers as current collector and Li_2S_6 as active material, a stable cycling performance of over 250 cycles without obvious capacity fading at 0.2C was achieved [36]. The cobalt atoms dispersed on hierarchical carbon nitride support was reported used as cathode electrocatalyst in lithium-polysulfide batteries by Wu et al. and a high discharge capacity of 800 mAh g^{-1} at 12.8 mA cm^{-2} was realized [37].

Herein, based on our previous works on oxygen vacancies [1,38], we report a novel fabrication “soft on rigid” hybrid fiber serving as self-supporting multifunctional cathode electrocatalyst. The hybrid consists of rigid Co–TiO_{2-x} fibers and soft CNF fibers which is mounted on its surface through subsequent chemical vapor deposition (CVD) techniques. A large amount of Co nanoparticles are coated in the CNF and abundant Co cluster attached on the surface of TiO_{2-x} (referred as Co–TiO_{2-x}/CNF). The “fiber on fiber” structure is designed to provide sufficient active sites for redox reaction. In addition, the CNF and unique structure lead to an enormous improvement in electron/ion transportation and overall electronic conductivity, which enhances the sulfur utilization and rate performance of sulfur cathodes. A large number of active sites were constructed by introducing oxygen vacancies on TiO_2. In addition, the introduced Co nano-clusters regulated the electronic structure, ion transport and reaction energy barrier of TiO_2, thus achieving improved polysulfide catalytic conversion ability and enhanced reaction kinetics. Due to these superiorities, the Li_2S_6/-Co–TiO_{2-x}/CNF cathode delivers an improved reversible capacity (1227 mAh g^{-1} at 0.1C after 100 cycles) and rate performance (743 mAh g^{-1} at 3.0C), demonstrating its superior electrochemical performance in Li–S batteries. In addition, calculations at the theoretical level and analysis at the experimental level are used to comprehensively explain the mechanism by which the electronic structure and the oxygen-defective structure synergistically regulate the catalytic activity mechanism and the enhancement of its ability to adsorb and convert LiPS.

2. Experimental

2.1. Synthesis

Preparation of the Co–TiO_{2-x}/CNF composite: Briefly, 0.281 g triblock copolymer Pluronic F127 and 0.4 g PVP (polyvinyl pyrrolidone, Mw = 1300000, Aldrich) were dissolved into 3.6 g ethanol under constant stirring for a uniform precursor solution. After while, 0.1925 g acetylacetone and 0.068 g pure water were put into the prepared precursor with stirring for 1 h. At last, 1.094 g of TTIP (Titanium isopropoxide) was put into the mixed solution under robust stirring at room temperature for 1 h, and then 0.286 g of cobalt nitrate hexahydrate was further added. Further stirring for 2 h was conducted to obtain an electrospinning solution. Afterwards the solution was loaded into a plastic syringe (5 mL) equipped with a capillary and needle head (0.7 mm in diameter). The working voltage was 8 kV, and the ejection rate of solution was 0.15 mm min^{-1}. An aluminum foil was employed to collect the precursor fibers with a distance of 20 cm from the nozzle. After electrospinning, CoO_x-TiO_2 precursor was subsequently heated at 280 °C for 2 h in air, and further calcination was conducted in Air at 600 °C for 1 h with a heating rate of 1 °C min^{-1}. As for the following CVD treatment, the CoO_x-TiO_2 was heated to 600 °C with a raising rate of 1 °C min^{-1} under Ar. And H_2 (10 mL min^{-1}) was introduced for 1 h with Ar (80 mL min^{-1}) at 600 °C. Subsequently, acetylene (10 mL min^{-1}) was introduced for 20 min with unchanged Ar/H_2 input to obtain Co–TiO_{2-x}/CNF. As a comparison, the TiO_2 precursor was prepared according to similar electrospinning process without the addition of cobalt nitrate hexahydrate. And the following calcination was conducted only in air.

Preparation of Li_2S_6 solution: Li_2S_6 (1 M) was prepared by adding Li_2S and S into 1.0 M lithium bis-trifluoromethanesulfonimide (LiTFSI) in 1,3-dioxolane (DOL) and 1,2-dimethoxyethane (DME) (1:1 by volume) including 1% $LiNO_3$ at a molar ratio of 1:5. Following constant mechanical stirring for 24 h at 60 °C was used to synthesize homogeneous Li_2S_6 electrolyte.

2.2. Materials characterization

X-ray diffraction (XRD, D8 Focus, Bruker) pattern was recorded by Cu Kα radiation. The morphology of the products was investigated by scanning electron microscopy (SEM, S-4800, Hitachi) and transmission electron microscopy (TEM, JEOL, JEM2100F). Raman spectra were measured in a Raman microscope (Thermo Scientific, Waltham, MA) with a laser excitation wavelength of 514 nm. Brunauer-Emmett-Teller (BET, V-Sorb, 2800P) was employed to test the specific surface area. X-ray photoelectron spectroscopy (XPS) spectra were recorded on a Thermal Fisher Scientific ESCALAB 250Xi spectrometer. To confirm the presence of vacancies, the g factor was determined using electron paramagnetic resonance (EPR, Bruker, A300) spectroscopy at 77 K.

2.3. Electrochemical measurements

The cathodes were fabricated by directly dropped the Li_2S_6 on the prepared Co–TiO_{2-x}/CNF. Coin-type cells (CR2032) were assembled by using the Li_2S_6/Co–TiO_{2-x}/CNF as cathode, lithium foil as anode, and Celgard 2400 polypropylene membrane as separator. The same procedures were used to prepare Li_2S_6/TiO_2 composite. The sulfur loading is controlled by the added amount of Li_2S_6. The electrolyte was 1.0 M LiTFSI dissolved in a 1:1 vol ratio of DOL and DME, containing 1% $LiNO_3$. The sulfur loading was calculated according to the molar mass of sulfur in Li_2S_6. 5 μL Li_2S_6 electrolyte (1 M) and 15 μL blank electrolyte were dropped in the Co–TiO_{2-x}/CNF electrode with a diameter of 9 mm, corresponding to the sulfur loadings of 1.5 mg cm^{-2} for regular test. The coin cells with high sulfur loading was assembled with different volume of Li_2S_6 electrolyte and blank electrolyte. The total amount of electrolyte

remains unchanged at 30 μL. The cells were assembled in an argon-filled glove box. Cyclic voltammetry (CV) curves and Nyquist plots were obtained using electrochemical workstation (Princeton, VersaSTAT 4). Galvanostatic charge and discharge tests were performed with a voltage window of 1.7–2.8 V on a Neware tester.

Symmetric cell: Sulfur powder and Li_2S were mixed with a molar ratio of 5:1 added into the above mentioned electrolyte to obtain the Li_2S_6 electrolyte. Co–TiO_{2-x}/CNF (TiO_2) was employed as the working electrode and the lithium foil was used as the counter electrode. CV measurements were tested on electrochemical workstation (Chenhua CHI–660C) from −1.5 V to 1.5 V at 10 mV s^{-1}.

Li_2S deposition measurement: Li_2S_8 electrolyte (0.25 mol L^{-1}) was prepared in a similar way to Li_2S_6 electrolyte, but using tetraglyme. The cell was galvanostatically discharged to 2.06 V at 0.112 mA, followed by discharging potentiostatically at 2.05 V.

Linear sweep voltammetry (LSV) measurement: The cells consisted of a working electrode, a reference (saturated Ag/AgCl electrode), and a counter electrode (platinum sheet). Li_2S/methanol solution (0.1 M) was used as electrolyte. The electrochemical workstation (Princeton, VersaSTAT 4) was employed to collect the results from −0.8 V to −0.3 V at 5 mV s^{-1}.

2.4. Computational method

The density functional theory (DFT) calculation was conducted using plane-wave ultra-soft pseudopotential method and Perdew-Burke-Ernzerhof (PBE) for the exchange and correlation energy terms. A 3 × 3 supercell of TiO_2 (101) surface was constructed and the vacuum height was set to 15 Å. The cut off energy of plane wave was 400 eV, and the Monkhorst-Pack grid k-space was set to be 2 × 2 × 1. The maximal interaction forces of atoms were 0.03 eV $Å^{-1}$.

3. Results and discussion

The ideal sulfur host needs to possess both strong adsorption ability on LiPSs and catalytic effect on sulfur species conversion. As above stated properties, DFT calculations were conducted to predict the possible structure, conductivity, adsorption and catalytic abilities to LiPSs of Co–TiO_{2-x}. Fig. 1a displays the optimized stable adsorption configurations and the corresponding binding energies of Li_2S_6 on the TiO_2, TiO_{2-x} and Co–TiO_{2-x} surfaces. The significantly increased binding energy due to the introduction of oxygen vacancies and Co cluster suggests the excellent chemical immobilization between Li_2S_6 and Co–TiO_{2-x}. The higher adsorption energy of Co–TiO_{2-x} could be attributed to the synergistic effect of Co–S bond caused from the introduced Co cluster and strengthened Ti–S bond by oxygen vacancies, which enhances the chemical affinity to LiPSs. Meanwhile, the modified TiO_2 further offers fast Li^+ diffusion capability on its surface, leading to much improved redox reaction (Fig. 1b). The Co–TiO_{2-x} exhibits a much lower Li^+ diffusion energy barrier of 0.88 eV than TiO_2 (1.48 eV) and TiO_{2-x} (1.22 eV), indicating its fast ion diffusion on Co–TiO_{2-x} surface. Apart from strong adsorption effect and fast Li^+ transfer, effective catalysis on the transformation of sulfur species is also important. The Li_2S deposition profiles in Fig. 1c performs a reduced Li_2S decomposition energy barrier of Co–TiO_{2-x} (0.67 eV) than that of TiO_2 (1.03 eV) and TiO_{2-x} (0.84 eV), indicating the fast LiPS conversion capability of oxygen vacancies and Co cluster. Therefore, the vast oxygen vacancies and Co cluster, serving as active sites, significantly strengthen the adsorption ability and catalytic conversion of LiPS, leading to much improved electrochemical performance.

In the practical application of Li–S battery, excellent conductivity is also important. Fig. 2a shows the density of states (DOS) patterns. TiO_2 and TiO_{2-x} all demonstrate distinct energy gaps for spin-up and spin-down channels with a typical semiconducting character. And the DOS pattern of TiO_{2-x} performs an extensive state rearrangement from TiO_2 along with the existence of a shallow donor level (defect level). After the introduction of Co cluster, the band gap disappeared, indicating the significantly improved electronic conductivity, which facilitates electron transportation within the electrode. Fig. 2b depicts the d-band centers. A highest Ti d-band center was found for Co–TiO_{2-x} (−0.02 eV) compared with that of TiO_2 (−0.22 eV) and TiO_{2-x} (−0.19 eV), especially the introduction of Co clusters significantly upshifts the d band center of

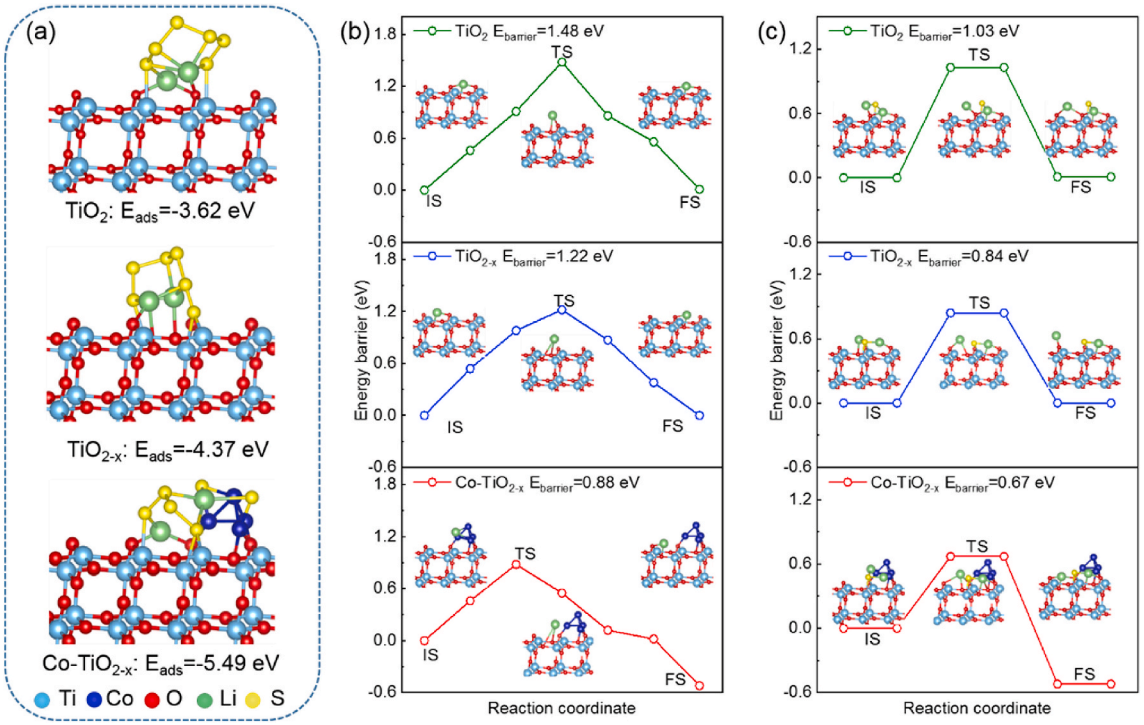

Fig. 1. (a) Chemical interactions between Li_2S_6 and TiO_2, TiO_{2-x} and Co–TiO_{2-x}; (b) the diffusion profiles of Li^+ on TiO_2, TiO_{2-x} and Co–TiO_{2-x}; (c) transition state of Li_2S decomposition on TiO_2, TiO_{2-x} and Co–TiO_{2-x}.

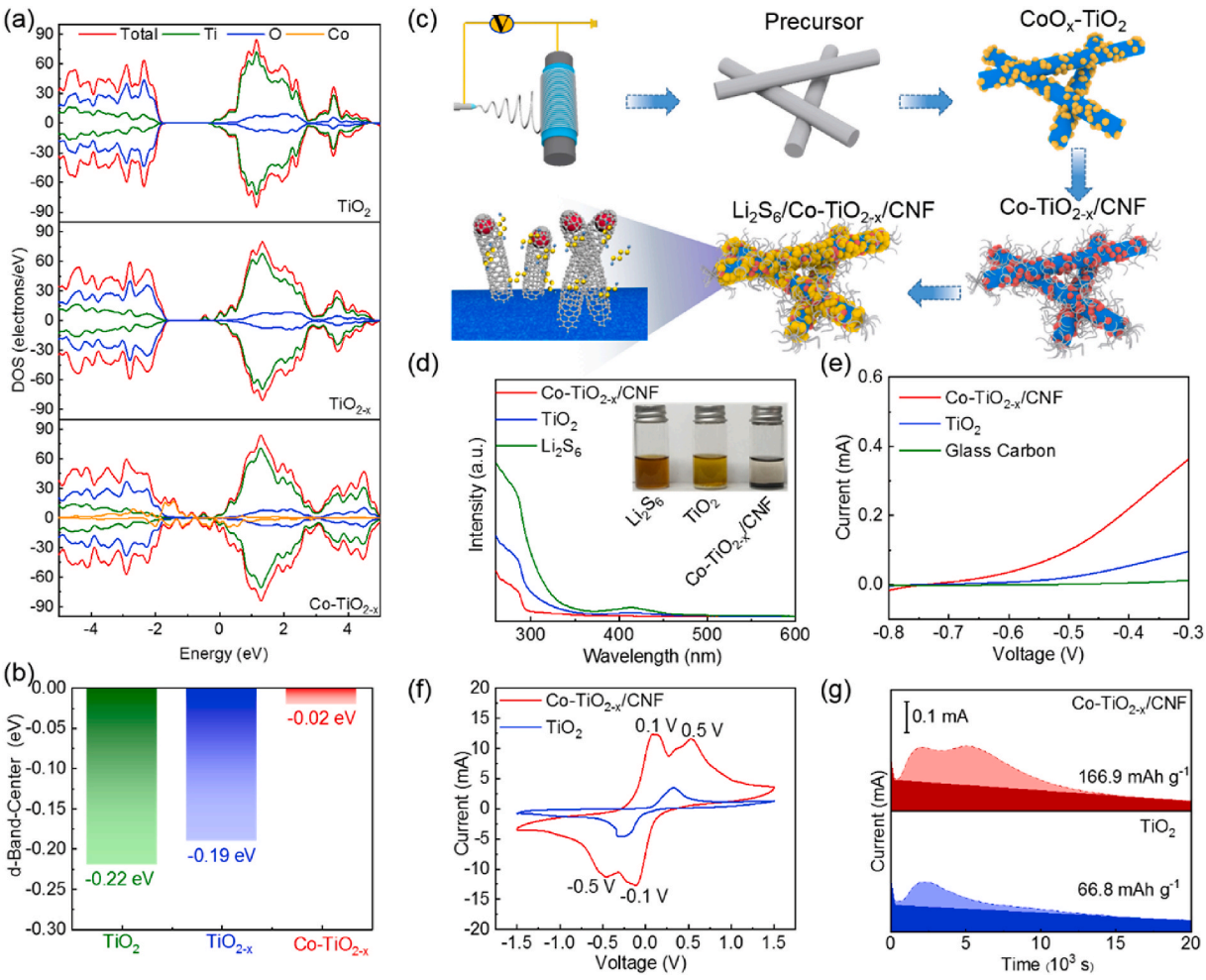

Fig. 2. (a) DOS profiles, (b) d-band center for Ti of TiO_2, TiO_{2-x} and Co–TiO_{2-x}; (c) schematic illustration of fabrication procedure for Li_2S_6/Co–TiO_{2-x}/CNF hybrid and the corresponding conversion mechanism. (d) UV–vis spectra and optical images (inset) of LiPS solution before and after adsorption by TiO_2 and Co–TiO_{2-x}/CNF; (e) LSV curves; (f) CV and (g) Li_2S deposition profiles of TiO_2 and Co–TiO_{2-x}/CNF.

Ti atoms, indicating that the Co cluster can regulate the Ti electronic structure and thereby improving the Li_2S_6 adsorbability.

In order to verify the practical effect, a Li_2S_6/Co–TiO_{2-x}/CNF hybrid was constructed to serve as sulfur host. The detailed fabrication procedure was shown in Fig. 2c. Co–TiO_{2-x}/CNF is composed of oxygen-deficient TiO_{2-x} rigid fiber decorated with Co cluster, soft CNF and the Co nanoparticles coated in the top of CNF. First, a homogeneous free-standing film precursor was achieved by using electrospinning technique. Then, the precursor was calcined in air to produce CoO_x-TiO_2 composite. After chemical vapor deposition (CVD) treatment, a Co–TiO_{2-x}/CNF film was obtained containing the metallic Co nanocrystals, TiO_{2-x} fiber and CNF fiber. In addition, Li_2S_6 was further loaded on the substrate by drop coating method to obtain the LiPS cathode.

The adsorption experiments with Li_2S_6 as the electrolyte were examined. The Li_2S_6 solution after adsorbed by Co–TiO_{2-x}/CNF became colourless, indicating its strong chemical affinity for Li_2S_6 attributed to the strong LiPS adsorption of Co–TiO_{2-x}/CNF, as seen in Fig. 2d. UV–vis spectroscopy was also employed to evaluate the LiPS adsorption capability of different sulfur immobilizer. After adsorption, the peak intensity at about 280 cm^{-1} and 415 cm^{-1} significantly reduced, corresponding to the decreasing concentration of S_6^{2-} and S_4^{2-} species, respectively. Furthermore, the accelerated electrocatalytic effect of Co–TiO_{2-x}/CNF was explored by the LSV test in Fig. 2e. A glass carbon was used as a reference electrode. The almost non-current response indicates that it has no effect on the sulfur oxidation process. The LSV curve of TiO_2 demonstrates an onset potential of ~ -0.5 V, which is lower than that of Co–TiO_{2-x}/CNF (−0.6 V). This evidence demonstrates the strong effect of Co–TiO_{2-x}/CNF on reducing the energy barrier of sulfur oxidation from solid Li_2S to soluble LiPS. Symmetric cells were employed to reveal the ability of Co–TiO_{2-x}/CNF on accelerating the LiPS transformation. The CV profiles are performed in Fig. 2f, distinctive and sharp peaks can be observed in Co–TiO_{2-x}/CNF, indicating its superiority to catalyze the conversion of LiPS due to the existence of oxygen vacancies and special electronic structures affected by introduced Co cluster. As a comparison, TiO_2 shows low current response, which is related to the limited LiPS catalytic conversion. Li_2S deposition profiles are shown in Fig. 2g to examine its Li_2S formation kinetics. The cell based on Co–TiO_{2-x}/CNF performs the stronger current response with the higher deposition capacity of 166.9 mAh g^{-1} than TiO_2 (66.8 mAh g^{-1}), indicating its better capability of boosting the transformation of LiPS into insoluble Li_2S.

To further explore the working mechanism, a series of characterizations were conducted to observe the properties of Co–TiO_{2-x}/CNF. The optical photos in Fig. S1 indicated its flexibility to serve as free-standing cathode. The SEM image in Fig. 3a reveals the morphology of the as-prepared precursor by electrospinning. The precursor consists abundant fibers with good size uniformity. After calcination in air, the uniform fiber structure of CoO_x-TiO_2 film is still maintained, as seen in Fig. 3b. After CVD treatment, abundant CNF fibers are loaded on the surface of TiO_{2-x}, which is capable to offer decent electronic conduction. A typical "soft on rigid" fiber structure is revealed in Fig. 3c and d. It is worth noting that no severe collapse occurred after the calcination and

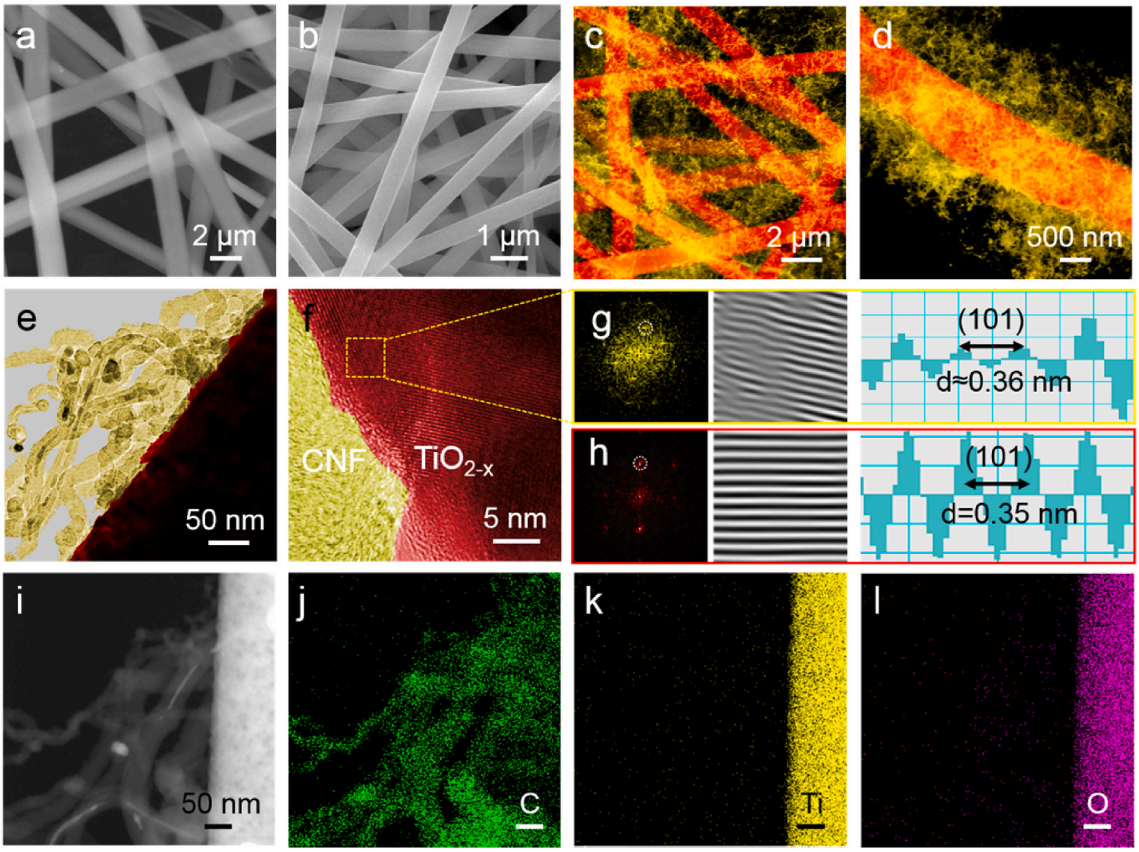

Fig. 3. SEM images of (a) precursor, (b) CoO_x-TiO_2; (c, d) Co–TiO_{2-x}/CNF; (e) TEM and (f) high-resolution TEM image of Co–TiO_{2-x}/CNF; (g, h) FFT pattern, inverse FFT pattern and lattice spacing images in the selected area; (i–l) high-magnification elemental mapping of Co–TiO_{2-x}/CNF.

CVD treatment. The thickness of the Co–TiO_{2-x}/CNF coating was determined by cross-sectional SEM to be about 37 μm in Fig. S2. The content of CNF in Co–TiO_{2-x}/CNF was explored to be 18.5% by TG under air atmosphere (Fig. S3). And the Co content in Co–TiO_{2-x}/CNF was calculated to be 0.67% by inductively coupled plasma-mass spectrometry. As comparison, Co–TiO_{2-x}/CNF with different Co contents is synthesized and the SEM images are shown in Figs. S4a–d. It can be seen that the limited Co addition in Co–TiO_{2-x}/CNF will result in reduced CNF loading, while excessive Co addition will collapse its unique structure.

The "soft on rigid" structure is confirmed by observation of the TEM image shown in Fig. 3e. As mentioned above, the Co–TiO_{2-x}/CNF is composed of TiO_{2-x} fiber, Co nanoparticles, and abundant CNF, which all can be clearly seen in Fig. 3e. In order to further observe the interface between the various components, selected area is performed in Fig. 3f. The interface between the CNF and TiO_{2-x} is clearly shown in Fig. 3f. In order to prove the existence of oxygen vacancy, the area in yellow frame is chosen to further explore using fast Fourier transform (FFT). The FFT results are shown in Fig. 3g, clear diffraction spots cannot be found, which demonstrates the arrangement of the crystal plane was severely damaged. Some dislocations can be seen in the inverse FFT result, which offers direct evidence that there are oxygen vacancies present in the Co–TiO_{2-x}/CNF composite. This is because some trivalent Ti atoms appear during the H_2-assisted reduction process. The Co–TiO_{2-x}/CNF composite consists of Ti_2O_3 (Ti^{3+}) and TiO_2 (Ti^{4+}), and these cause the composite to become disordered and to have some oxygen vacancies [39]. The lattice spacing of 0.36 nm further confirms the defective nature of the obtained TiO_{2-x} by showing a slightly expanded interplanar spacing on the (101) face. The HRTEM result of TiO_2 without oxygen vacancy (Fig. S5) is used as a comparison, the area in red frame is chosen to further explore using FFT. The FFT result is shown in Fig. 3h, clear and bright diffraction spots are obtained, indicating the excellent crystallinity of TiO_2. After the inverse FFT treatment, distinct lattice fringes are revealed, which is attributed to the (101) plane of TiO_2. TEM elemental mapping analysis indicates that the uniform elemental distribution in Co–TiO_{2-x}/CNF (Fig. 3i-l). In order to prove the existence of Co cluster, the selected area of Fig. 3f was analyzed in Fig. S6. The lattice spacing in HRTEM and corresponding FFT patterns in Fig. S6 not only confirms the existence form of metallic Co, but also reveals its ultrafine size in Co–TiO_{2-x}/CNF. Meanwhile, In Fig. S7, a HRTEM image exhibits a fringe spacing of the Co (111) plane and the outer CNF coating, which also indicates the existence of Co in the Co–TiO_{2-x}/CNF. The Co cluster on the surface of TiO_{2-x} can regulate the d-band center of Ti towards improved LiPSs adsorbability and enhance electronic conductivity, rendering much improved redox reaction kinetics.

The crystallization properties of the samples were analyzed by XRD patterns in Fig. 4a. Obviously, the diffraction peak of Co–TiO_{2-x}/CNF at 26.7° originated from the CNF, which was deposited via CVD treatment. In addition, the XRD pattern showed several diffraction peaks which were indexed to the (101), (004), (200), (211), and (004) planes of anatase TiO_2 (PDF#21–1272). However, compared with the pattern of TiO_2, there is a down-shift toward smaller angles for Co–TiO_{2-x}/CNF, especially in the range of 20–30° because of the presence of oxygen vacancies [40,41]. Furthermore, there are no obvious diffraction peaks of Co were found, indicating its limited content in the composite. BET test was conducted to observe the porosity of the samples. The Co–TiO_{2-x}/CNF exhibits a much higher Barrett-Emmett-Teller surface area of 132.7 $m^2\ g^{-1}$ than TiO_2 (81.5 $m^2\ g^{-1}$), confirming the success of CNF loading on the TiO_2 fibers (Fig. 4b). The higher surface area is able to stockpile sulfur and uniform the sulfur distribution, leading to improved electrochemical performances of Li–S batteries. Raman spectra were measured to investigate the graphitization degree of Co–TiO_{2-x}/CNF, and the results are shown in Fig. 4c. The as-prepared

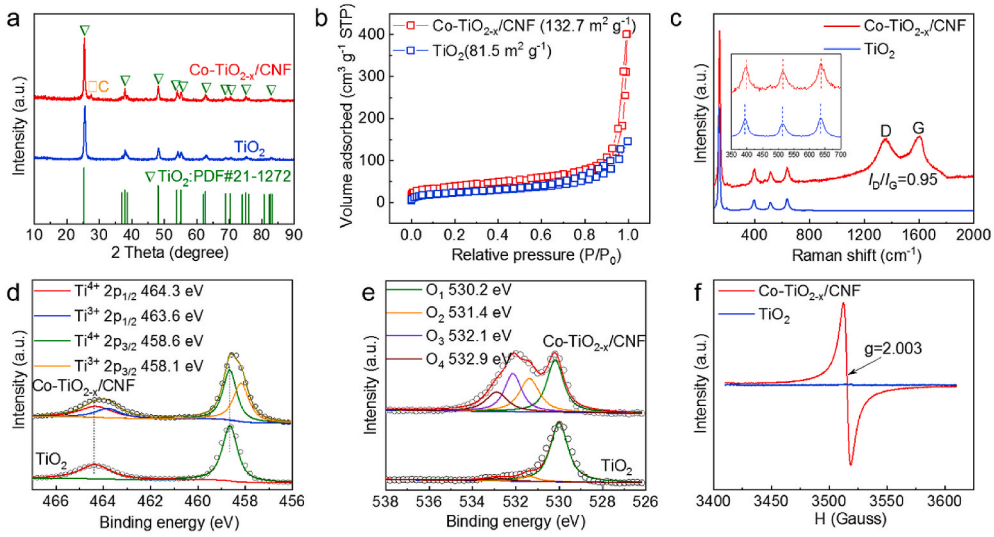

Fig. 4. (a) XRD patterns, (b) Nitrogen adsorption isotherms, (c) Raman spectra, (d) Ti 2p and (e) O 1s high-resolution XPS spectra, (f) EPR spectra of TiO_2 and Co–TiO_{2-x}/CNF.

Co–TiO_{2-x}/CNF exhibits two typical peaks at 1351 and 1602 cm^{-1}, and these are ascribed respectively to the D-band and G-band vibrations of carbonaceous material. The intensity ratio of the D-band to the G-band (I_D/I_G) for Co–TiO_{2-x}/CNF is 0.95, and this indicates the partial graphitization degree of the CNF that formed because of the introduction of the cobalt catalyst. Furthermore, the TiO_2 peaks, which located at 141 cm^{-1}, 391 cm^{-1}, 514 cm^{-1} and 634 cm^{-1}, are shifted to higher wavenumber in Co–TiO_{2-x}/CNF, and this further proves the presence of oxygen vacancies in the Co–TiO_{2-x}/CNF [42]. XPS spectra of the composites were recorded and analyzed. The Ti 2p XPS spectrum proves the generation of Ti^{3+}, corresponding to a pair of smaller peaks at 458.1 and 463.6 eV (Fig. 4d). A reducing H_2 atmosphere was introduced via CVD and should promote the formation of Ti^{3+} sites and adjacent oxygen vacancies that would accelerate electron transportation within the oxide. Therefore, the presence of Ti^{3+} sites greatly improves the conductivity of the Co–TiO_{2-x}/CNF composite [41,43]. Moreover, the O 1s XPS spectrum also verifies the existence of oxygen vacancies (Fig. 4e). The O_3 peak located at 532.1 eV is attributed to the generation of oxygen

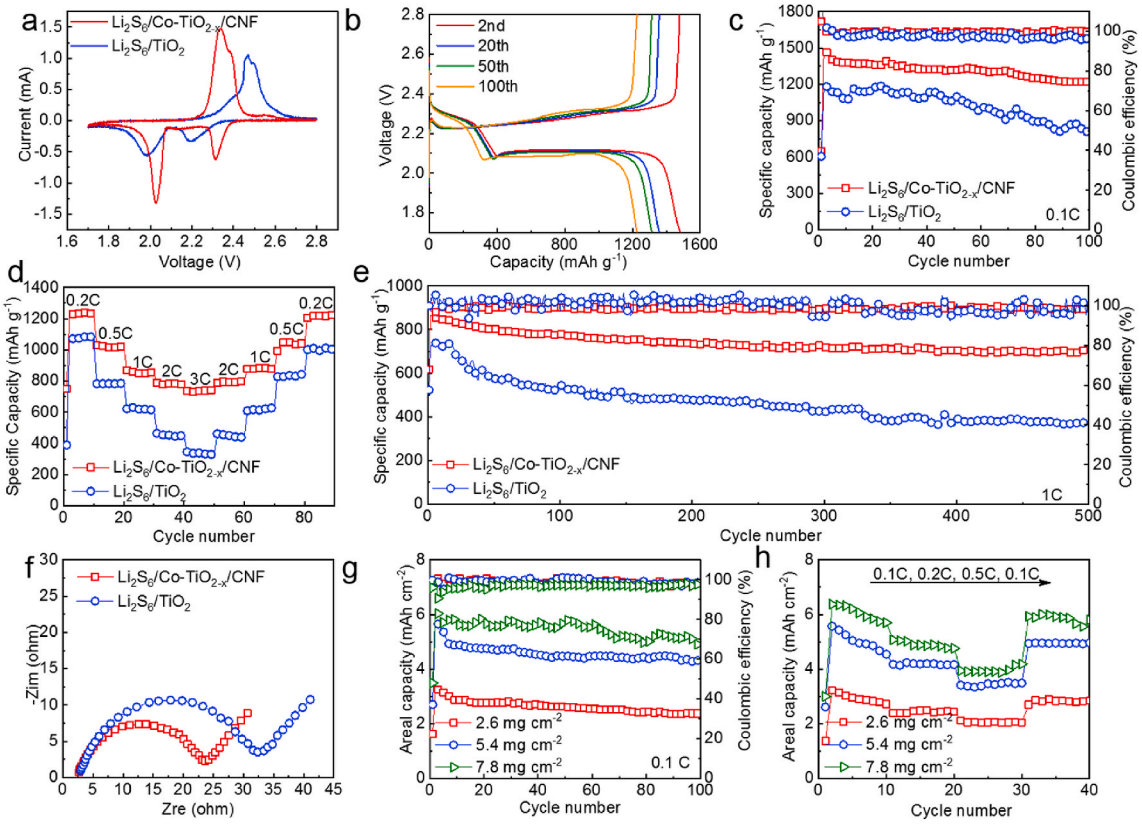

Fig. 5. (a) CV, (b) charge-discharge profiles, (c) cycle performance of Li_2S_6/Co–TiO_{2-x}/CNF cathode, (d) rate capability, (e) long-term operation and (f) EIS of various electrodes, (g) high-loading and lean-electrolyte performances and (h) rate capability of Li_2S_6/Co–TiO_{2-x}/CNF cathode.

vacancies. And the O_1 peak at 530.2 eV represents the Ti–O bond, the O_2 peak at 531.4 eV is contributed by the O–H bond. The O_4 peak at 532.9 eV is caused by adsorbed moisture [40,44]. The existence of oxygen vacancies is also verified by EPR measurements, in which the Co–TiO_{2-x}/CNF produces a distinctive EPR signal with a g factor of 2.003 (Fig. 4f), corresponding to electrons localized on oxygen vacancies and implying that H_2-assisted reduction largely increased the concentration of oxygen vacancies.

Based on above mechanism analysis, it was proved that Co–TiO_{2-x} shows the superior catalytic performance. In order to verify this, electrochemical performance of CR2032-type coin cells with Li_2S_6/TiO_2 and Li_2S_6/Co–TiO_{2-x}/CNF cathodes were measured. Fig. 5a shows cyclic voltammetry (CV) curves. For each cycling process, both the Li_2S_6/TiO_2 and Li_2S_6/Co–TiO_{2-x}/CNF cathodes undergo typical two-step reduction reactions and a one-step oxidation reaction. The cathodic peaks can be explained as the reduction of sulfur (S_8) to soluble high-order lithium polysulfides (Li_2S_x, $4 \leq x \leq 8$) and its further reduction to Li_2S_2/Li_2S while the anodic peaks are related to the oxidation of Li_2S_2/Li_2S to S_8 [45,46]. Moreover, comparing with the Li_2S_6/TiO_2 cathode, the Li_2S_6/Co–TiO_{2-x}/CNF cathode witness a much lower potential hysteresis, indicating its improved Li–S electrochemistry. Fig. 5b shows the galvanostatic charge-discharge curves of the Li_2S_6/Co–TiO_{2-x}/CNF cathode at 0.1C. The galvanostatic charge-discharge curves indicate that the Li_2S_6/Co–TiO_{2-x}/CNF electrode shows obvious charge/discharge plateaus, which is consistent with the CV curves. The potential hysteresis (ΔE) of the Li_2S_6/Co–TiO_{2-x}/CNF cathode is small, indicating its low electrochemical polarization and excellent reversibility.

Fig. 5c displays the cycling performance of the Li_2S_6/TiO_2 and Li_2S_6/Co–TiO_{2-x}/CNF cathodes at 0.1C. After 100 cycles, the Li_2S_6/Co–TiO_{2-x}/CNF and Li_2S_6/TiO_2 cathodes exhibit discharge capacities of 1227 and 796 mAh g^{-1}, respectively. The Li_2S_6/Co–TiO_{2-x}/CNF cathode has a higher capacity and capacity retention during the cycling process. In order to explore the structure stability of Co–TiO_{2-x}/CNF under the repeated cycling process, the electrode after cycling was further investigated, as shown in Fig. S8. The SEM image and element mapping reveal a distinctive "soft on rigid" fibrous structure with a uniform element distribution after cycling, indicating the superior structure stability of Co–TiO_{2-x}/CNF to serve as multifunctional sulfur immobilizer for fast and durable Li–S performance. The rate performance of the cells with the Li_2S_6/Co–TiO_{2-x}/CNF and Li_2S_6/TiO_2 cathodes were assessed from 0.2C to 3.0C (Fig. 5d). The specific capacity of the Li_2S_6/Co–TiO_{2-x}/CNF cathode is 1234 mAh g^{-1} at 0.2C (the 10th cycle), whereas the corresponding value for the Li_2S_6/TiO_2 cathode is 1081 mAh g^{-1} (the 10th cycle). At higher C-rates set for 0.5C, 1.0C, 2.0C and 3.0C (the 10th cycle), the specific capacities of Li_2S_6/Co–TiO_{2-x}/CNF cathode yields 1018, 853, 781 and 743 mAh g^{-1}, respectively. Furthermore, a high reversible capacity of 1203 mAh g^{-1} is still recovered at 0.2C after cycles, indicating the improved rate performance caused by Co–TiO_{2-x}/CNF.

The long cycle performance at 1C was further tested to prove the cycling stability of the Li_2S_6/Co–TiO_{2-x}/CNF cathode at 1.0C for up to 500 cycles. As seen in Fig. 5e, a high capacity of 694 mAh g^{-1} after 500 cycles with a low capacity fade of only 0.03% per cycle can be obtained in Li_2S_6/Co–TiO_{2-x}/CNF cathode, indicating its much improved capacity retention. Such good cycling stability is attributed to a synergistic effect of the 3D interwoven structure and defective structure design of Co–TiO_{2-x}/CNF, which exhibit high electrical conductivity, strong LiPS adsorption and fast trapping-conversion. EIS spectra of various electrodes are shown in Fig. 5f. Clearly, the Li_2S_6/Co–TiO_{2-x}/CNF cathode shows the lower charge transfer resistance, indicating the rapid charge transport and accelerated sulfur redox reactions.

The practical application of Li–S batteries requires a stable operation under high sulfur loading and decreased electrolyte/sulfur (E/S) ratio. Therefore, the cells with different mass loading and electrolyte content were evaluated to validate the excellence catalytic effect of Co–TiO_{2-x}/CNF electrocatalyst. As demonstrated in Fig. 5g, the specific discharge capacities of the Li_2S_6/Co–TiO_{2-x}/CNF cathodes under different sulfur loadings of 2.6, 5.4, and 7.8 mg cm^{-2} can keep a satisfying discharge capacity of 2.4, 4.3, and 4.8 mAh cm^{-2} after 100 cycles, respectively. Even under raised sulfur loading of 7.8 mg cm^{-2}, a high capacity retention is still retained. Besides, at 7.8 mg cm^{-2}, the rate performance displays a high areal capacity of 4 mAh cm^{-2} at 0.5C, proving the enhanced sulfur utilizations as well as reduced electrochemical polarization (Fig. 5h). Attributed to its structural superiorities, the remarkable performance enhancement of Co–TiO_{2-x}/CNF was achieved when serving as cathode electrocatalyst.

4. Conclusions

In summary, we successfully fabricated oxygen-deficient and Co cluster decorated Co–TiO_{2-x}/CNF as efficient cathode electrocatalyst for Li–S batteries. Compared with Li_2S_6/TiO_2, the Li_2S_6/Co–TiO_{2-x}/CNF cathode shows a superior cycling stability with a reversible capacity of 694 mAh g^{-1} (capacity decay of only 0.03% per cycle) after 500 cycles at 1.0C. The enhanced electrochemical performance of Li_2S_6/Co–TiO_{2-x}/CNF can be attributed to *i)* introduced Co clusters upshift the d-band center of Ti atoms and thereby improving the Li_2S_6 adsorbability of TiO_{2-x}; *ii)* the strengthened physical confinement offered by its unique structure and strong chemical interactions given by oxygen vacancies and Co cluster; *iii)* the promoted LiPS adsorption and conversion kinetics by the unique electronic structures regulated by Co cluster. This combination of defect structure design and electronic structure adjustment promotes the development of cathode electrocatalyst for Li–S batteries toward fast and durable Li–S redox reaction, holding great promises to be utilized as multifunctional cathode substrate and electrocatalyst toward its practical applications.

CRediT authorship contribution statement

Jiayi Wang: Conceptualization, Investigation, Data curation, Writing - original draft. **Dan Luo:** Conceptualization, Writing - review & editing, Supervision. **Junhua Li:** Conceptualization, Methodology, Data curation. **Yongguang Zhang:** Resources, Conceptualization, Supervision, Writing - review & editing, Project administration, Funding acquisition. **Yan Zhao:** Resources, Conceptualization, Supervision, Writing - review & editing, Project administration, Funding acquisition. **Guofu Zhou:** Resources, Conceptualization, Supervision, Writing - review & editing, Project administration, Funding acquisition. **Lingling Shui:** Resources, Conceptualization, Supervision, Writing - review & editing, Project administration, Funding acquisition. **Zhongwei Chen:** Resources, Conceptualization, Supervision, Writing - review & editing, Project administration, Funding acquisition. **Xin Wang:** Resources, Conceptualization, Supervision, Writing - review & editing, Project administration, Funding acquisition.

Declaration of competing interest

The authors declare that they have no known competing financial interests or personal relationships that could have appeared to influence the work reported in this paper.

Acknowledgment

This work was supported by the Program for the Outstanding Young Talents of Hebei Province, China (YG.Z.); Chunhui Project of Ministry of Education of the People's Republic of China (Grant No. Z2017010); Xijiang R&D Team (X.W.); Guangdong Innovative and Entrepreneurial Team Program (No. 2016ZT06C517); Science and Technology Program of Guangzhou (No. 2019050001); Science and Technology Program of Zhaoqing (No. 2019K038). The authors also thank the support from Natural Sciences and Engineering Research Council of Canada, University of Waterloo, and Waterloo Institute for Nanotechnology.

Appendix A. Supplementary data

Supplementary data to this article can be found online at https://doi.org/10.1016/j.nanoen.2020.105293.

References

[1] D. Wang, Q. Cao, B. Jing, X.Y. Wang, T.L. Huang, P. Zeng, S.X. Jiang, Q. Zhang, J. Y. Sun, Chem. Eng. J. 399 (2020) 125723.
[2] Y.G. Zhang, Y. Zhao, A. Konarov, D. Gosselink, H.G. Soboleski, P. Chen, J. Power Sources 241 (2013) 517–521.
[3] Y.X. Yin, S. Xin, Y.G. Guo, L.J. Wan, Angew. Chem. Int. Ed. 52 (2013) 13186–13200.
[4] Z.W. Seh, Y.M. Sun, Q.F. Zhang, Y. Cui, Chem. Soc. Rev. 45 (2016) 5605–5634.
[5] R.P. Fang, S.Y. Zhao, Z.H. Sun, D.W. Wang, H.M. Cheng, F. Li, Adv. Mater. 29 (2017) 1606823.
[6] D. Aurbach, B.D. McCloskey, L.F. Nazar, P.G. Bruce, Nat. Energy 1 (2016) 16128.
[7] Y. Tian, G.R. Li, Y.G. Zhang, D. Luo, X. Wang, Y. Zhao, H. Liu, P.G. Ji, X.H. Du, J. D. Li, Z.W. Chen, Adv. Mater. 32 (2019) 1904876.
[8] Q. He, B. Yu, H. Wang, M. Rana, X.B. Liao, Yan Zhao, Nano Res. 13 (2020) 2299–2307.
[9] G.M. Zhou, E. Paek, G.S. Hwang, A. Manthiram, Nat. Commun. 6 (2015) 7760.
[10] L. Ma, H.L. Zhuang, S. Wei, K.E. Hendrickson, M.S. Kim, G. Cohn, R.G. Hennig, L. A. Archer, ACS Nano 10 (2016) 1050–1059.
[11] Z. Li, H.B. Wu, X.W. Lou, Energy Environ. Sci. 9 (2016) 3061–3070.
[12] P. Zeng, H. Yu, M.F. Chen, W.S. Xiao, Y.F. Li, H. Liu, J. Luo, J. Peng, D.S. Shao, Z. Y. Zhou, Z.G. Luo, Y. Wang, B.B. Chang, X.Y. Wang, J. Energy Chem. 51 (2020) 21–29.
[13] J. Sun, H.W. Lee, M. Pasta, H.T. Yuan, G.Y. Zheng, Y.M. Sun, Y.Z. Li, Y. Cui, Nat. Nanotechnol. 10 (2015) 980–985.
[14] A. Manthiram, S.H. Chung, C.X. Zu, Adv. Mater. 27 (2015) 1980–2006.
[15] M.F. Chen, X.M. Zhao, Y.F. Li, P. Zeng, H. Liu, H. Yu, M. Wu, Z.H. Li, D.S. Shao, C. Q. Miao, G.R. Chen, H.B. Shu, Y. Pei, X.Y. Wang, Chem. Eng. J. 385 (2020) 123905.
[16] L. Ma, K.E. Hendrickson, S. Wei, L.A. Archer, Nano Today 10 (2015) 315–338.
[17] W. Kang, N. Deng, J. Ju, Q. Li, D. Wu, X. Ma, L. Li, M. Naebe, B. Cheng, Nanoscale 8 (2016) 16541–16588.
[18] H.W. Chen, C.H. Wang, Y.F. Dai, S.Q. Qiu, J.L. Yang, W. Lu, L.W. Chen, Nano Lett. 15 (2015) 5443–5448.
[19] P. Wang, Z.A. Zhang, X.L. Yan, M. Xu, Y.X. Chen, J.M. Li, J. Li, K. Zhang, Y.Q. Lai, J. Mater. Chem. A 6 (2018) 14178–14187.
[20] R.Q. Liu, Y.J. Liu, J. Chen, Q. Kang, L.L. Wang, W.X. Zhou, Z.D. Huang, X.J. Lin, Y. Li, P. Li, X.M. Feng, G. Wu, Y.W. Ma, W. Huang, Nano Energy 33 (2017) 325–333.
[21] P. Zeng, M.F. Chen, S.X. Jiang, Y.F. Li, X. Xie, H. Liu, X.Y. Hu, C. Wu, H.B. Shu, X. Y. Wang, ACS Appl. Mater. Interfaces 11 (2019) 22439–22448.
[22] H.J. Peng, J.Q. Huang, M.Q. Zhao, Q. Zhang, X.B. Cheng, X.Y. Liu, W.Z. Qian, F. Wei, Adv. Funct. Mater. 24 (2014) 2772–2781.
[23] Y. Tian, Z.H. Sun, Y.G. Zhang, X. Wang, Z. Bakenov, F.X. Yin, Nanomaterials 8 (2018) 50.
[24] X. Qian, L. Jin, D. Zhao, X. Yang, S. Wang, X. Shen, D. Rao, S. Yao, Y. Zhou, X. Xi, Electrochim. Acta 192 (2016) 346–356.
[25] T.Y. Lei, W. Chen, J.W. Huang, C.Y. Yan, H.X. Sun, C. Wang, W.L. Zhang, Y.R. Li, J. Xiong, Adv. Energy Mater. 4 (2017) 1601843.
[26] H. Pan, X.X. Huang, R. Zhang, D. Wang, Y.T. Chen, X.M. Duan, G.W. Wen, Chem. Eng. J. 358 (2019) 1253–1261.
[27] Y. Xia, H. Zhong, R. Fang, C. Liang, Z. Xiao, H. Huang, Y. Gan, J. Zhang, X. Tao, W. Zhang, J. Power Sources 378 (2018) 73–80.
[28] G. Xu, B. Ding, L. Shen, P. Nie, J. Han, X. Zhang, J. Mater. Chem. A 1 (2013) 4490–4496.
[29] Z.W. Seh, W.Y. Li, J.J. Cha, G.Y. Zheng, Y. Yang, M.T. McDowell, P.C. Hsu, Y. Cui, Nat. Commun. 4 (2013) 1331.
[30] C.L. Dai, J.M. Lim, M.Q. Wang, L.Y. Hu, Y.M. Chen, Z.Y. Chen, H. Chen, S.J. Bao, B. L. Shen, Y. Li, G. Henkelman, M.W. Xu, Adv. Funct. Mater. 28 (2018) 1704443.
[31] L.F. Duan, L.J. Zhao, H. Cong, X.Y. Zhang, W. Lv, C.L. Xue, Small 15 (2019) 1804347.
[32] Q. Pang, X. Liang, C.Y. Kwok, L.F. Nazar, Nat. Energy 1 (2016) 16132.
[33] Z.B. Xiao, Z. Yang, L. Wang, H.G. Nie, M. Zhong, Q.Q. Lai, X.J. Xu, L.J. Zhang, S. M. Huang, Adv. Mater. 27 (2015) 2891–2898.
[34] H.C. Wang, C.Y. Fan, Y.P. Zheng, X.H. Zhang, W.H. Li, S.Y. Liu, H.Z. Sun, J. P. Zhang, L.N. Sun, X.L. Wu, Chem. Eur J. 23 (2017) 9666–9673.
[35] L. Qie, C.X. Zu, A. Manthiram, Adv. Energy Mater. 6 (2016) 1502459.
[36] C.Q. Shang, L.J. Cao, M.Y. Yang, Z.Y. Wang, M.C. Li, G.F. Zhou, X. Wang, Z.G. Lu, Energy Storage Mater. 18 (2019) 375–381.
[37] J. L. Wu, J. M. Chen, Y. Huang, K. Feng, J. Deng, W. Huang, Y. L. Wu, J. Zhong, Y. G. Li, 64 (2019) 1875-1880.
[38] D. Luo, Z. Zhang, G.R. Li, S.B. Cheng, S. Li, J.D. Li, R. Gao, M. Li, S. Sy, Y.P. Deng, Y. Jiang, Y.F. Zhu, H.Z. Dou, Y.F. Hu, A.P. Yu, Z.W. Chen, ACS Nano 14 (2020) 4849–4860.
[39] Z. Wang, C. Yang, T. Lin, H. Yin, P. Chen, D. Wan, F. Xu, F. Huang, J. Lin, X. Xie, M. Jiang, Energy Environ. Sci. 6 (2013) 3007–3014.
[40] D. Luo, G.R. Li, Y.P. Deng, Z. Zhang, J.D. Li, R.L. Liang, M. Li, Y. Jiang, W. W. Zhang, Y.S. Liu, W. Lei, A.P. Yu, Z.W. Chen, Adv. Energy Mater. 13 (2019) 1900228.
[41] D.D. Guan, Q. Yu, C. Xu, C.J. Tang, L. Zhou, D.Y. Zhao, L.Q. Mai, Nano Res. 10 (2017) 4351–4359.
[42] J. Chen, Z. Ding, C. Wang, H. Hou, Y. Zhang, C. Wang, G. Zou, X. Ji, ACS Appl. Mater. Interfaces 8 (2016) 9142–9151.
[43] G.J. Jeong, J.G. Kim, M.S. Park, M. Seo, S.M. Hwang, Y.U. Kim, Y.J. Kim, J.H. Kim, S.X. Dou, ACS Nano 8 (2014) 2977–2985.
[44] G.X. Liu, W. Li, R. Bi, C.A. Etogo, X.Y. Yu, L. Zhang, ACS Catal. 8 (2018) 1720–1727.
[45] X. Tao, J. Wang, C. Liu, H. Wang, H. Yao, G. Zheng, Z.W. Seh, Q. Cai, W. Li, G. Zhou, C. Zu, Y. Cui, Nat. Commun. 7 (2016) 11203.
[46] J.Q. Huang, Q. Zhang, H.J. Peng, X.Y. Liu, W.Z. Qian, F. Wei, Energy Environ. Sci. 7 (2014) 347–353.

Jiayi Wang received his Master degree in School of Material Science and Engineering from Hebei University of Technology and now he is a Ph.D candidate at South China Normal University. His research is currently focused on novel electrode materials and rechargeable lithium-sulfur batteries.

Dr. Dan Luo received his Ph.D degree in Chemical Engineering from University of Waterloo and now he is a postdoctoral fellow under the supervision of Prof. Zhongwei Chen at the University of Waterloo. His research is currently focused on the development of novel electrode materials, structures and electrolyte for rechargeable lithium-sulfur batteries and solid-state lithium batteries.

Junhua Li received her Master degree in School of Material Science and Engineering from Hebei University of Technology. Her research is currently focused on rechargeable lithium-sulfur batteries.

Yongguang Zhang is an Associate Professor of School of Materials Science and Engineering at Hebei University of Technology, China. He received his BS and Master degree in Chemical Engineering from Tianjin University, and earned his Ph.D in Chemical Engineering at University of Waterloo in 2013. His current interests include the synthesis and characterization of nanomaterials for energy storage and conversion, especially for lithium-ion batteries and lithium/sulfur batteries.

Yan Zhao received her Master degree in Chemical Engineering from University of Waterloo. Currently, she is a lab technician at the Hebei University of Technology. Her current research focuses on the nanostructured materials for energy applications.

Prof. Guofu Zhou is a China National Distinguished Professor in the field of micro/nano optoelectronic materials, devices and flat panel displays at South China Normal University (SCNU) and Co-founder & Director of Electronic Paper Display Institute of SCNU, National Center for International Research on Green Optoelectronics and joint research labs of SCNU-TUE, -UT and -UG. He is currently leading several national research projects and Sino-Dutch joint projects. Prof. Zhou is winner of the ISMANAM-1994 Best Young Scientist Gold Medal and Philips "Gilles Holst" Award for the year 2006.

Prof. Lingling Shui received her Ph.D degree in Electrical Engineering from Twente University (2009), the Netherlands. She is now a full professor at South China Academy of Advanced Optoelectronics & School of Information and Optoelectronic Science and Engineering, South China Normal University. Her research interests are fundamentals and applications based on microfluidics and electrofluidic technologies, especially for sensors, actuators and displays.

Dr. Zhongwei Chen is Canada Research Chair Professor in Advanced Materials for Clean Energy at the University of Waterloo, the Fellow of the Royal Society of Canada, the Fellow of the Canadian Academy of Engineering and Vice President of International Academy of Electrochemical Energy Science (IAOEES). His research interests are the development of advanced energy materials and electrodes for fuel cells, metal-air batteries, and lithium-ion batteries. He has published 2 book, 9 book chapters and more than 300 peer reviewed journal articles with over 28,000 citations with a H-index of 83 (GoogleScholar).

Prof. Xin Wang received his Ph.D degree from Beijing Normal University at 2012. After that, Dr. Wang work in University of Waterloo (Canada) as a postdoc fellow and then he joined South China Normal University (China). He has been working on electrochemistry technology for energy conversion and storage, including electrocatalysis, photocatalysis, Li-ion batteries, Li–S battery and other energy storage materials and devices.